Differential cross sections for collisions of hexapole state-selected NO with He

A. Gijsbertsen, H. Linnartz,[a] G. Rus, A. E. Wiskerke, and S. Stolte[b]
Laser Centre and Department of Physical Chemistry, Vrije Universiteit Amsterdam, De Boelelaan 1083, 1081 HV Amsterdam, The Netherlands

D. W. Chandler
Combustion Research Facility, Sandia National Laboratory, Livermore, California 94550

J. Kłos[c]
Departamento de Quimica Fisica, Facultad de Quimica, Universidad Complutense, 28040 Madrid, Spain

(Received 30 August 2005; accepted 28 September 2005; published online 12 December 2005)

The first measurements of differential inelastic collision cross sections of fully state-selected NO ($j=1/2$, $\bar{\Omega}=1/2$, $\epsilon=-1$) with He are presented. Full state selection is achieved by a 2 m long hexapole, which allows for a systematic study of the effect of parity conservation and breaking on the differential cross section. The collisionally excited NO molecules are detected using a resonant $(1+1')$ REMPI ionization scheme in combination with the velocity-mapped, ion-imaging technique. The current experimental configuration minimizes the contribution of noncolliding NO molecules in other rotational states $j,\bar{\Omega},\epsilon$ —that contaminates images— and allows for study of the collision process at an unprecedented level of detail. A simple method to correct ion images for collision-induced alignment is presented as well and its performance is demonstrated. The present results show a significant difference between differential cross sections for scattering into the upper and lower component of the Λ-doublet of NO. This result cannot be due to the energy splitting between these components. © *2005 American Institute of Physics*. [DOI: 10.1063/1.2126969]

I. INTRODUCTION

Detailed knowledge of rotationally inelastic collisions is of great importance in understanding energy transfer between molecules and atoms. The study of collisions of rare gases with (open shell) NO molecules has been used in the past to characterize inelastic collisions and reactions. In the last decades much work has been reported on this subject. Early work on He–NO and Ar–NO collisions[1] resulted in integral inelastic cross sections and showed that these exhibit an oscillatory structure as a function of the final rotational state. Large anisotropy effects in the Ar–NO and He–NO potential were found by De Lange *et al.*[2–4] In their experiments NO molecules were oriented, after which the integral state-to-state collision cross section was determined using laser induced fluorescence (LIF). Typically, LIF provides only integral cross sections, while differential cross sections are nowadays usually obtained using ion-imaging techniques. Suits *et al.*[5] were the first to apply the latter technique to obtain differential cross sections for collisions of Ar with NO. The introduction of this technique triggered new research, especially after Eppink and Parker[6] improved the achievable resolution considerably with the implementation of electrostatic lenses. The velocity-mapped ion-imaging technique is now commonly used in the field of molecular dynamics.[7–15] Differential cross sections for inelastic collisions can also be measured using a movable detector,[16] but this technique is more time consuming and experimentally difficult. The resolution depends on the scattering angle and only the scattering angle of the molecule in the laboratory frame can be obtained. Velocity-mapped ion-imaging provides the velocity vector of the scattered molecules (both its absolute value and the scattering angle).

Potential energy surfaces (PESs) govern chemical reactions. There is, however, no method to measure them directly, although some attempts were made to directly calculate potential energy surfaces from measured differential cross sections.[17,18] In practice, theoreticians calculate PESs for a certain system, use the PESs to calculate differential cross sections (DCSs) and then compare the DCSs to experimental values as a test. The first measurement of inelastic differential cross sections for He–NO collisions was carried out by Wesley *et al.*[19] and compared to scattering calculations based on the Yang and Alexander CEPA PESs.[20] The measurements showed in all cases more forward scattering than the calculations. Also Kohguchi *et al.*[21] reported discrepancies between theory and experiment for Ar–NO differential cross sections. Elioff *et al.*[11] repeated these measurements for spin-orbit changing collisions and found a better correspondence to theory for the ratio between forward- and backward-scattered molecules than in Kohguchi's work.

The experiment described in this work is the first scattering experiment in which differential cross sections for

[a]Present address: Sackler Laboratory for Astrophysics, Leiden Observatory, The Netherlands.
[b]Author to whom correspondence should be addressed. Fax +31 20 5987643. Electronic mail stolte@few.vu.nl
[c]Present address: Department of Chemistry and Biochemistry, University of Maryland, College Park, MD 20742.

scattering from a single Λ-doublet state are obtained. The molecules are prepared in a single quantum state before the collision and the detection of the scattered molecules is also fully state selective. This experiment provides the first opportunity to take a close look at the effect of parity breaking and parity conservation on the differential cross section. A hexapole state selector[22,23] is used to select the NO molecules in the low field seeking upper component of the Λ-doublet with symmetry index $\epsilon=-1$. It works as a positive lens for molecules in the low field seeking component, while it diverges molecules in the high field seeking lower component of the Λ-doublet with $\epsilon=1$.

All previous crossed-beam ion-imaging work relies on adiabatic expansion alone for the initial state preparation. Besides resolving the Λ-doublet of the NO molecules in the beam, hexapole state selection suppresses the percentage of incoming molecules in higher rotational states ($j>1/2$) into the scattering center. These molecules are less deflected by the hexapole and are not focused into the scattering region, but undergo (passive) divergence over the length of the hexapole. The hexapole selected beam of molecules allows for measurements of differential cross sections for low final rotational states that were previously unmeasurable due to the presence of molecules in these rotational states in the beam, that obscured the forward scattered intensity.

Collision-induced alignment has been shown to influence ion images[24] and thus the values of the differential cross sections that are extracted from these images. Wade *et al.*[13] used vertical and horizontal laser polarization to determine the NO alignment after collision and used the alignment information to correct the differential cross sections. In our study, a simple, yet rigorous, method to cope with collision-induced alignment is presented. The conservation of the projection m_a of the total angular momentum on the kinematic apse is exploited for alignment correction. Apse quantization was proposed and demonstrated to be a feasible approximation by Khare *et al.*[25] Later on, Meyer *et al.* showed that the apse approximation yields good quantitative results for (among others) He–NO collisions[26] and Ne–NO collisions.[27]

II. EXPERIMENT

In order to explore Λ-state selected differential cross sections, a previously used crossed-beam apparatus[2,4,23,28] has been modified. The existing LIF detection system is replaced by newly designed ion optics for velocity-mapped ion-imaging. A XeCl excimer pumped dye laser system (Lambda Physik EMG 201/FL 3002) is used for detection. The dye laser operates with Coumarin 47 dye and is equipped with a frequency doubling unit to generate tunable light around $\lambda\approx226$ nm (output $\leqslant$1.5 mJ/pulse). The excimer laser generates around 90 mJ of $\lambda=308$ nm light of which approximately 10% is separated using a small mirror in front of the dye laser and is used in the ionization step of the $(1+1')$ resonance enhanced multiphoton ionization (REMPI) process.[29] As the excimer beam is rather divergent, a telescope consisting of an $f=100$ mm and an $f=-50$ mm lens is placed immediately after the mirror that reflects the 10%. The focus of this beam is made to coincide with the scattering center using an $f=300$ mm lens. The $\lambda\approx226$ nm laser beam is not focused, but guided through an iris with a diameter of about 1 mm. The excitation and ionization beams are crossed at 90° to get a well defined ionization volume, estimated to be 1 mm^3. When the tunable laser light is blocked, no signal can be observed, meaning that nonresonant ionization of NO in the ground state does not occur. When the $\lambda=308$ nm ionization laser beam is blocked, the signal is typically less than 10% of that when both laser beams are on. As there is competition between $(1+1)$ and $(1+1')$ REMPI, the contribution of $(1+1)$ REMPI to the signal is expected to be suppressed even more than 10%.

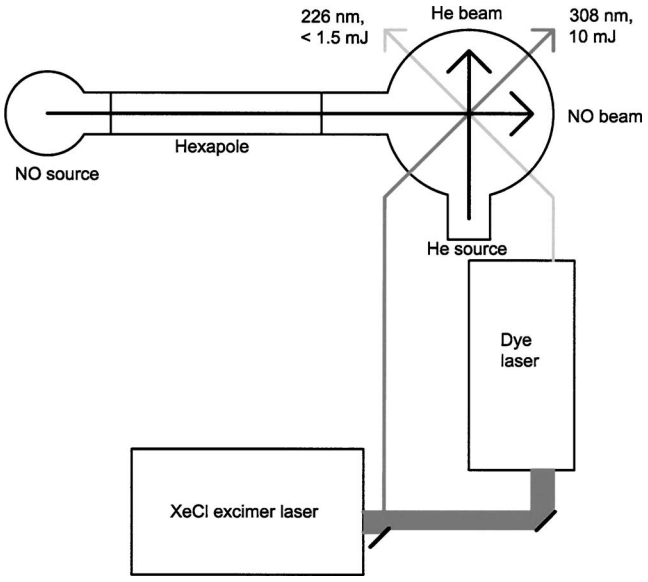

FIG. 1. Schematic drawing of the crossed-beam ion-imaging setup. The time-of-flight tube is perpendicular to the plane defined by the laser and molecular beams and points upwards.

The main advantages of using $(1+1')$ REMPI in the crossed laser configuration are that it generates a well defined and rather isotropic detection volume and that it is less likely that the 308 nm light ionizes background molecules in the vacuum chamber than the 226 nm light. The small isotropic volume simplifies the extraction of differential cross sections from ion-images and reduces distortion of the images due to ionization near the edges of the electrostatic lenses. Using 308 nm light for ionization, the 226 nm light intensity can be reduced, which decreases the noise level. For most background gas molecules the 308 nm photon is below the ionization threshold. Using $(1+1')$ REMPI it is possible to overcome saturation in the excitation step, whereas the ionization step is saturated.

A schematic drawing of the experimental setup is shown in Fig. 1. The primary beam consists of 16% NO in Ar, the secondary beam of pure He. Both beams are produced using general valves, pulsed at a frequency of 10 Hz. The NO in the primary beam is rotationally cold due to adiabatic expansion, i.e., most of the NO molecules are in the lowest rotational state with angular momentum quantum number $j=1/2$. The beam passes two skimmers ($\oslash=1$ mm and $\oslash=0.7$ mm) that are situated 3 and 8 cm from the pulsed nozzle opening, respectively, before it enters the hexapole.

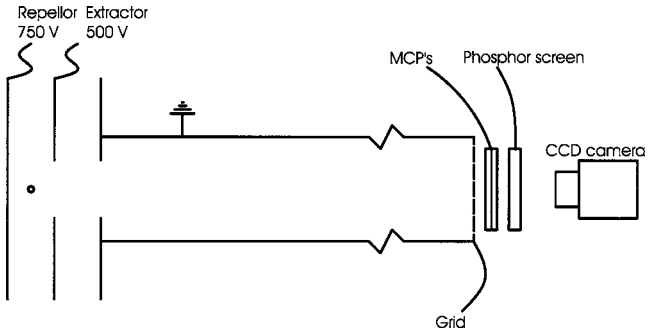

FIG. 2. Schematic drawing of the ion optics. The crossing point of the molecular and laser beams is indicated by a small circle. The TOF tube is placed perpendicularly (pointing upwards) to the plane defined by the laser and molecular beams.

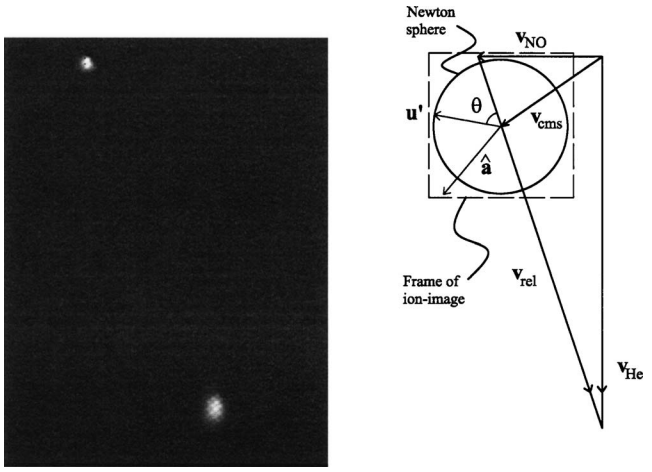

FIG. 3. The left panel shows an ion image of two "beam spots." The top left spot is from the 16% NO beam in Ar beam (593 m/s), while the lower spot is due to the 1% NO in He beam velocity (1710 m/s). The camera is positioned such that the up-down direction of the ion-images coincides with the axis of the He beam, the right-left direction coincides with that of the NO beam. The right panel shows the corresponding Newton diagram. The vector $\boldsymbol{u}'$ indicates scattering with a velocity u' in the center-of-mass frame under an angle θ. The corresponding kinematic apse direction is indicated by $\hat{\boldsymbol{a}}$. Note that the u' distribution after collision is (cylindrically) symmetric around the relative velocity $\boldsymbol{v}_{rel}$. The dashed square indicates the frame of the recorded ion images that remains unaltered for all images in Figs. 4–6. The center-of-mass originis shifted downwards along v_{rel} (by 0.07 v_{rel}) of to enhance the readability of the figure. This leads to a Newton sphere that is too large.

The 2 m long hexapole focuses molecules in the low field seeking $(\epsilon=-1,f)$ upper component of the lambda doublet into the detection/collision region.[22] In the collision region, the NO beam is crossed at 90° with a He beam. The He nozzle is positioned 8.5 cm from the scattering center, the beam of He atoms is collimated by a ($\oslash$=1.9 mm) skimmer, positioned 1.5 cm from the nozzle. During the experiments (both beams on) the ion gauge pressure reading in the collision chamber is approximately $1\cdot10^{-6}$ mbar.

Because of hexapole focusing, the state-selected NO beam is very pure. Only the molecules in the $j=1/2$, $\bar{\Omega}=1/2$, $\epsilon=-1$ state are focused. The $(1+1')$ REMPI signal difference (hexapole gain) when tuning the dye to the focused ground state between "hexapole on" and "hexapole off" is approximately a factor of 70. The contribution of the other component of the Λ-doublet is negligible as it is diverged by the hexapole.[2] The amount of molecules in other quantum states is substantially less than 1%. Switching on the He beam does not weaken the ground-state signal significantly, from which it can be concluded that less than 2% of the NO molecules collide. The contribution of double collisions can thus be ignored.

The ion optics and time-of-flight (TOF) tube are placed perpendicularly to the drawing plane of Fig. 1 and a schematic drawing is given in Fig. 2. The distance between the repeller and extractor plates is 20 mm and the length of the TOF tube amounts to 550 mm. The TOF tube is at ground, the "back" of the microchannel plate (MCP) detector (facing the phosphor screen) is at 950 V while the "front" (facing the grid) is gated to a negative voltage (−950 V). A grid (transmission of 90%) is positioned just before the MCPs. This grid prevents ions from being pulled towards the center of the detector when the front voltage is switched to −950 V. Simulations show that without the grid, the resolution decreases and that the molecular velocity component (before ionization) perpendicular to the TOF is no longer linear with the position of impact on the detector. This problem cannot be solved by putting the front of the MCPs at ground and gate the back at +2 kV. In that case the NO^+ ions would have less kinetic energy (600 V instead of 1.6 kV) when they hit the detector, yielding weak signals. Low repeller voltages are essential to facilitate the resolution required for detection of the small changes in NO velocity due to collisions with the light He atoms. Disturbances of the images because of the inhomogeneous field in the region near the detector are avoided using the grid in front of the detector. The ions see two parallel plates and are accelerated perpendicularly to the detector. The grid shows up in some images, but the effect on the differential cross sections is negligible.

To test and optimize the setup, about 1% NO was added to the He beam. Optimal repeller and extractor voltages are determined with NO in both the primary and in the secondary beam. The dye laser (226 nm) is tuned to the electronic transition starting from the $j=1/2$, $\bar{\Omega}=1/2$, $\epsilon=-1$ state. Repeller and extractor voltages were tuned to the value at which the beam spots were as small as possible[15] and at which the primary (NO) and secondary (He) beam were on the horizontal and vertical axis, respectively. In Fig. 3 the resulting image is shown that was recorded after optimization of the voltages. Typical values used throughout this work are 750 V for the repeller and 500 V for the extractor. Lower values of 500 V and 330 V can be applied successfully as well. The image in Fig. 3 provides information on the properties of the molecular beams. The resolution of the setup is determined from the (primary) NO-beam. Its velocity has been calculated and measured before.[2,3] Using the value of 593 m/s, a resolution G of 7.7 m/s per pixel is found. The secondary beam is found to be a little slower than calculated for pure He (1710 m/s instead of 1760 m/s). This is assumed to be due to the 1% of NO that was added to facilitate detection. The full width at half maximum (FWHM) of the velocity distribution of the (primary) NO beam and the (secondary) He beam are estimated to be, respectively, 50 and 100 m/s (along the beam velocity). The velocity spread in the He

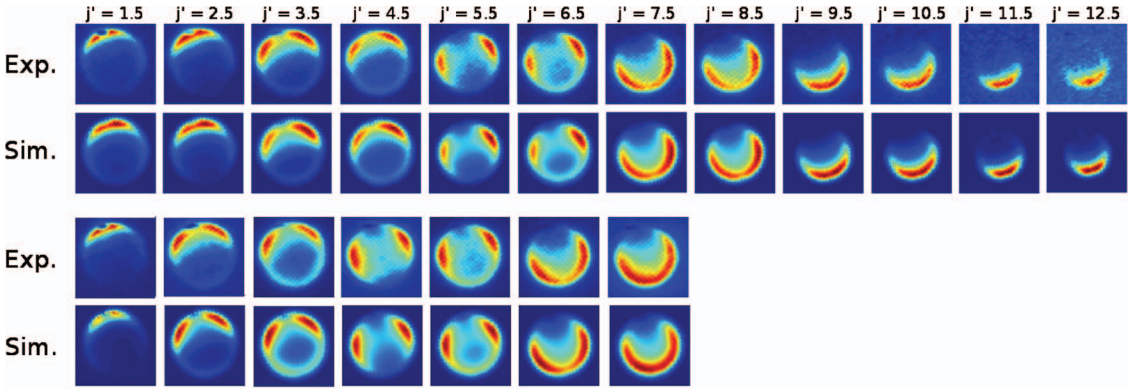

FIG. 4. (Color) Experimental and simulated ion images. The images in the top rows are collected using the R_{21} branch ($\bar{\Omega}'=1/2$, $\epsilon'=-1$). The bottom rows show images collected using the P_{11} branch ($\bar{\Omega}'=1/2$, $\epsilon'=1$). The experimental images are raw data, the simulated images are from the optimized extracted differential cross section and incorporate blurring, velocity correction $T(x,y)$, and alignment correction $S_a(j'\rightarrow j^*)$. No saturation correction is applied: $S_0=0$. The frames of all images are identical and taken in accordance to the dashed square in the right panel of Fig. 3.

beam is probably underestimated because only the 1% NO seeded in He is actually detected and not the lighter He itself.

Knowing the velocities of the NO and the He beams, a Newton diagram is drawn to yield insight in the collision geometry (right panel of Fig. 3). The centers of the beam spots in the left panel of Fig. 3 correspond to the $\boldsymbol{v}_{\mathrm{NO}}$ and $\boldsymbol{v}_{\mathrm{He}}$ vectors in the right panel. For laboratory velocities the symbol "v" will be used, while "u" indicates a velocity in the center-of-mass frame. The $\boldsymbol{u}'$ distribution after collision is (cylindrically) symmetric around the relative velocity $\boldsymbol{v}_{\mathrm{rel}}$. This scattering (Newton) sphere of the NO molecules is projected on the detector. For reasons of readability the scattering sphere for He is not drawn in the figure. The dashed square in the right panel of Fig. 3 denotes the frame of the ion images, as used for all images in Figs. 4–6.

III. EXTRACTION OF DIFFERENTIAL CROSS SECTIONS

The detection probability of a scattered molecule depends on several factors. This makes it impossible to directly use the intensity on an outer ring of an ion image to determine the differential cross section. Asymmetries in the images can occur due to collision-induced rotational alignment, due to different residence times for slow and fast molecules within the detection volume and due to the Doppler shifts and laser alignment. The beam velocity distributions and instrumental factors cause blurring of the images. In this section, a method is given to correct for the most important of these distorting factors in order to extract reliable differential cross sections from the ion images in a straightforward procedure.

Currently no corrections for imperfect spatial positioning of the laser and for Doppler shift are applied to our data as the effect of these factors was found to be small. The center-of-mass velocity distribution of the NO molecules after collision ($\boldsymbol{u}'$) is small compared to the bandwidth of the laser (0.5 cm^{-1}). Hardly any change of the asymmetry of the images was observed when slightly detuning the frequency of the dye laser.

The blurring of the ion images due to the velocity spread in the beams as well as other instrumental factors is approximated by a single Gaussian blurring function. This function is fitted empirically to a computer generated image in order to match the sharpness of the experimental images.

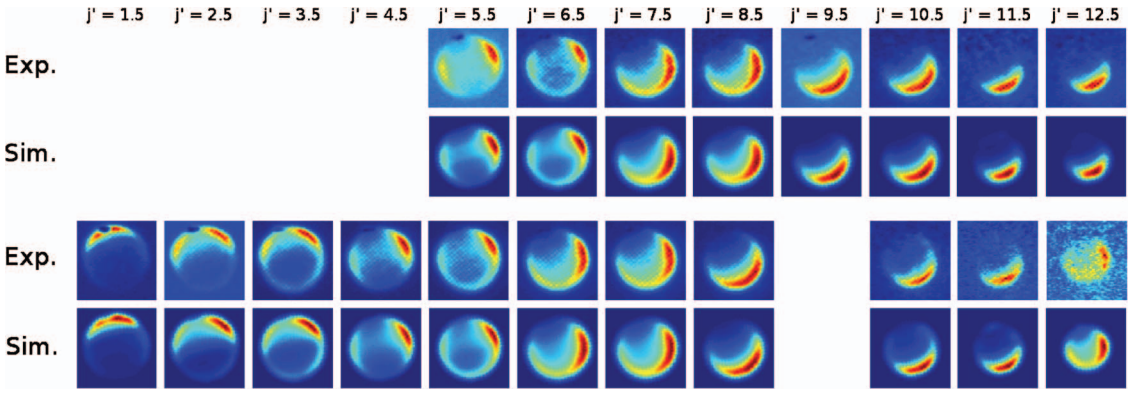

FIG. 5. (Color) Experimental and simulated ion images. The images in the top rows are collected using the $Q_{11}+P_{21}$ branch ($\bar{\Omega}'=1/2$, $\epsilon'=-1$). The bottom rows show images collected using the $R_{11}+Q_{21}$ branch ($\bar{\Omega}'=1/2$, $\epsilon'=1$). The experimental images are raw data, the simulated images are adapted using blurring, velocity correction $T(x,y)$ and alignment correction $S_{\mathrm{sat}}(j'\rightarrow j^*)$. Partial saturation was included to reproduce the asymmetry: $S_0\approx 1.5\langle S_a(j'\rightarrow j^*)\rangle$ where $\langle S_a(j'\rightarrow j^*)\rangle$ is the mean value of the alignment correction, averaged over all pixels. An "unsaturated" image would show even stronger asymmetry. The frames of all images are identical and taken in accordance to the dashed square in the right panel of Fig. 3.

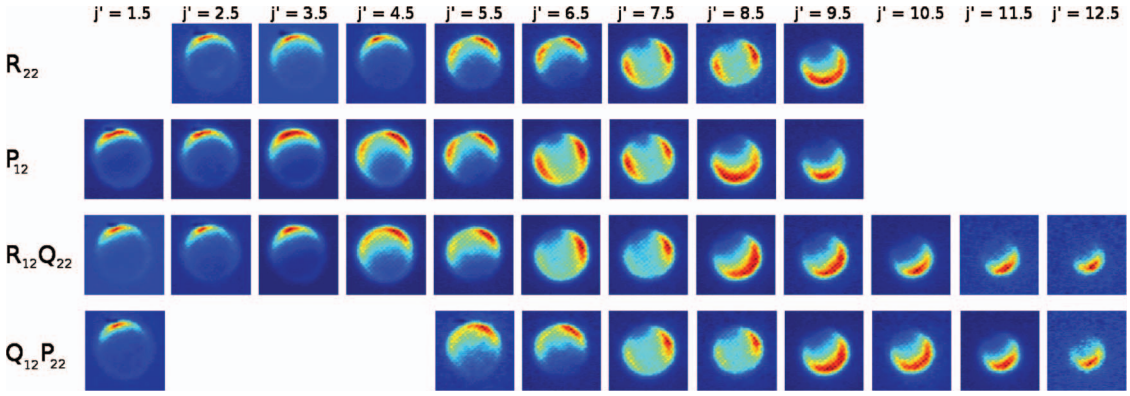

FIG. 6. (Color) Experimental (raw) ion images for spin-orbit changing ($\bar{\Omega}'=3/2$) collisions. Simulated images from the extraction of the differential cross section are not presented for these branches, but correspond to the experimental images as well as in the case of spin-orbit conserving collisions. The frames of all images are identical and taken in accordance to the dashed square in the right panel of Fig. 3.

The detection region is defined by four crossing beams: The NO beam, the He beam and the two laser beams, each with a diameter of about one millimeter. It is an experimental challenge to overlap all four beams in time as well as in space. The resulting detection volume is small which restricts the maximally achievable signal. The advantages of this geometry, however, are that the ionization volume is nearly spherical and that due to the small detection volume relative to the size of the ion lenses edge effects from the latter are minimized. Because of the nearly spherical shape of the detection volume we make the approximation that the molecular detection probability $T(x,y)$ due to the molecule's residence time in the detection volume is inversely proportional to the absolute value of the velocity in the laboratory frame. The coordinates (x,y) indicate the position on the detector in pixels and relate directly to the x and y components of the velocity in the center-of-mass (u'_x and u'_y) frame via the resolution G ($x=u'_x/G$ and $y=u'_y/G$) with unit $m/s/pixel$.

$$T(x,y) \equiv \frac{1}{|\boldsymbol{v}'|} \Big/ \left\langle \frac{1}{|\boldsymbol{v}'|} \right\rangle. \tag{1}$$

Normalization of this $T(x,y)$ is obtained by dividing with the average over all pixels ($\langle 1/|\boldsymbol{v}'|\rangle$). Appendix A shows the procedure to calculate $T(x,y)$. If the detection volume would be nonisotropic or not centered at the beam crossing, $T(x,y)$ will also depend on the (laboratory) scattering-angle. For example: Molecules scattered along a single laser (LIF or (1+1) REMPI)[3] have a longer pathway through the detection volume than those scattered in another direction. If this were the case, an extra correction would be required.

Collision-induced alignment can also cause NO molecules to be nonuniformly detected, creating a further distortion of the ion image, which has to be corrected for. The alignment dependent detection probability is given by:

$$S_a(j' \to j^*) \equiv \sum_{m^*} |\langle \Psi^*(j^*,m^*)|\hat{\boldsymbol{\mu}}\cdot\hat{\boldsymbol{\varepsilon}}|\boldsymbol{R}(\beta_p)\Psi'_a(j',m'_a)\rangle|^2. \tag{2}$$

The wave functions are referred to as $\Psi'_a(j',m'_a)$ and $\Psi^*(j^*,m^*)$, denoting, respectively, that of a rotational state after collision and that after laser excitation to the $A\,^2\Sigma^+$ state. Note that m^* is defined along the polarization $\hat{\boldsymbol{\epsilon}}$ of the linearly polarized laser (laser frame). The wave function in the apse system $\Psi'_a(j',m'_a)$ (m'_a is defined along the kinematic apse) is transformed into the laser frame by the Euler angle rotation operator $\boldsymbol{R}(\beta_p)\equiv\boldsymbol{R}(0,\beta_p,0)$. The angle between the laser polarization and the kinematic apse is given by β_p. Since $S_a(j'\to j^*)$ depends on β_p, it is not an ordinary Hönl-London factor. The scattered wave function can carry alignment, while the Hönl-London factors assume an isotropic m distribution. Until now no simple method to calculate $S_a(j'\to j^*)$ for each position (x,y) on the detector was available. Appendix B provides a simple but widely applicable correction treatment based on the approximate conservation of the projection m_a of the total angular momentum $\boldsymbol{j}$ on the kinematic apse ($m'_a=m_a$). It results in a value of $S_a(j'\to j^*)$ for every position on the detector. Khare[25] and Meyer[26] showed that m_a conservation is an appropriate assumption. $S(j'\to j^*)$ is evaluated for every pixel with coordinate (x,y) on the detector.

In the case of full saturation of the excitation step, the detection probability no longer depends on the scattering angle. Correction of the ion images with only the velocity correction should in this case yield images that are symmetric in the relative velocity. If partial saturation occurs, the dependence of the detection probability on β_p becomes less

$$S_{\mathrm{sat}}(j'\to j^*) = S_0 + S_a(j'+j^*). \tag{3}$$

The parameter S_0 indicates the saturation: when $S_0 \ll S_a(j'\to j^*)$, there is no saturation, when $S_0 \gg S_a(j'\to j^*)$ there is full saturation and the detection probability $S_{\mathrm{sat}}(j'\to j^*)$ no longer depends on the scattering angle. To get an idea of the effect of the saturation correction, S_0 can be expressed in units of $\langle S_a(j'\to j^*)\rangle$, the value of $S_a(j'\to j^*)$ averaged over all pixels.

In order to actually extract differential cross sections from the ion images, first the experimental image $I_{\mathrm{ex}}(x,y)$ is corrected for the laboratory velocity and alignment via Eqs. (1) and (2). For more information on the correction, see Appendixes A and B. The corrected image is given by

TABLE I. Branches used to collect ion images, indicating which $\bar{\Omega}', \epsilon'$ states (after collision) are probed. For each of the branches, images for several j' (up to $j'=12.5$) are collected.

Branch	$\bar{\Omega}'$	ϵ'
P_{11}	1/2	1
R_{21}	1/2	−1
P_{12}	3/2	1
R_{22}	3/2	−1
$R_{11}+Q_{21}$	1/2	1
$P_{21}+Q_{11}$	1/2	−1
$R_{12}+Q_{22}$	3/2	1
$P_{22}+Q_{12}$	3/2	−1

$$I_{\mathrm{ex},c}(x,y) = \frac{I_{\mathrm{ex}}(x,y)}{S_a(j' \rightarrow j^*)T(x,y)}. \quad (4)$$

In the case of (partial) saturation, $S_a(j' \rightarrow j^*)$ is replaced by $S_{\mathrm{sat}}(j' \rightarrow j^*)$. The corrected image is now reasonably symmetric (but still blurred) and the intensity on the rim of the ion image already gives a good indication of the differential cross section. To obtain a proper differential cross section (DCS) from the blurred two-dimensional velocity distribution of the corrected image, a forward extraction method is applied. This method is in the spirit of Lorenz *et al.*[7] The intensity $R_{\mathrm{ex}}(\theta)$ on an about 6 pixels wide outer ring of the corrected ion image $I_{\mathrm{ex},c}(x,y)$ is used as a "trial DCS" $[\mathrm{DCS}_0=R_{\mathrm{ex}}(\theta)]$ to simulate an image. The blurring factor—that includes both the beam velocity distribution and instrumental blurring—is applied on the simulated image to make it as sharp as the corrected experimental image $I_{\mathrm{ex},c}(x,y)$. The intensity on a broad outer ring of the simulated image $R_{\mathrm{sim}}(\theta)$ is compared to that of the same outer ring on the experimental image $(R_{\mathrm{ex}}(\theta))$, after which the DCS is adapted.

$$\mathrm{DCS}_i = \frac{R_{\mathrm{sim},i-1}(\theta)}{R_{\mathrm{ex}}(\theta)}\mathrm{DCS}_{i-1}. \quad (5)$$

Note that $R_{\mathrm{sim},i-1}$ has been simulated using DCS_{i-1}. The adapted trial DCS is used to simulate an image that is compared with the experimental one. This step is repeated several times $(i=1,2,3,\ldots)$ until the simulated and experimental images are as similar as possible. Two parameters have to be fitted during the optimization. The saturation parameter S_0 is chosen such that the asymmetry of the corrected experimental image is minimized, while the Gaussian blurring parameter is selected to make the simulated image as sharp as the experimental one.

IV. CLOSE-COUPLING CALCULATIONS OF DIFFERENTIAL CROSS SECTIONS

The calculations of the differential cross sections were done using a full quantum close-coupling (CC) approach with two diabatic potentials $[V_{\mathrm{sum}}=\frac{1}{2}(A''+A')$ and $V_{\mathrm{dif}}=\frac{1}{2}(A''-A')]$ for the He–NO$(X\,^2\Pi)$ system taken from Ref. 30. The contour plots of the diabatic surfaces are shown in Refs. 4 and 30. Calculations of the steric dependence of the inelastic total collision cross section using these surfaces yielded a reasonably good agreement with experimental data.[4]

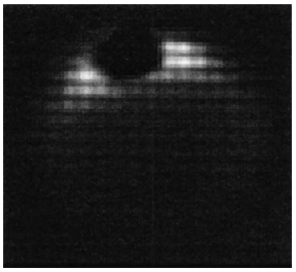

FIG. 7. Ion image for $j=1/2$, $\epsilon=-1 \rightarrow j'=1/2$, $\epsilon'=1$ scattering $(R_{11}+Q_{21}$ branch). The black spot is due to background subtraction. This background signal is due to the small amount of molecules that still resides in this state (the lower component of the Λ-doublet) after the hexapole. This image was recorded under different imaging conditions.

The HIBRIDON suite of codes[31] was used for the scattering calculations. The methodology of scattering of the structureless partner with an open shell diatomic was described in detail before.[4,21,27,32–36] We refer the reader to these references for details. The close-coupling calculations at a collision energy $E_{\mathrm{col}}=508.13\ \mathrm{cm}^{-1}$ employed all partial waves up to a total angular momentum quantum number $J_{\mathrm{max}}=101.5$ and NO rotational levels up to $j'=17.5$. The reduced mass of the He–NO system and the rotational constant of the NO molecule were taken as $\mu=3.5314$ a.m.u. and $B=1.696\ 11\ \mathrm{cm}^{-1}$, respectively.

The description of the NO diatomic can be done in a Hund's case (a) coupling scheme. This is due to the relatively large spin-orbit coupling resulting in $^2\Pi_{1/2}$ (ground-state spin-orbit manifold F_1) and $^2\Pi_{3/2}(F_2)$. Each spin-orbit state is further split into Λ-doublet components with symmetry index $\epsilon=1(e)$ and $\epsilon=-1(f)$. Λ-doubling parameters, p and q for NO are $1.172\cdot10^{-2}$ and 6.7×10^{-4}, respectively. For the spin-orbit Hamiltonian $A*\hat{L}\hat{S}$ a spin-orbit constant of the NO molecule of $A=123.1393\ \mathrm{cm}^{-1}$ has been used.

The CC equations were propagated from $R=3.7-35\ a_0$. From the CC calculations we were able to determine integral and differential cross sections for state-to-state transitions from the $j=0.5$ initial state of NO, resolved for Λ-doublet and spin-orbit manifold (F_1 and F_2). The integral cross sections from these calculations are used to normalize the experimental results in this study.

V. RESULTS AND DISCUSSION

A nearly complete set of ion images for inelastic He–NO collisions at a collision energy of approximately 510 cm^{-1} is displayed in Figs. 4–6. The raw experimental images are shown. In Figs. 4 and 5 the raw experimental images are compared to simulated images from the extraction of differential cross sections, including the corrections discussed in Sec. III. A few images are missing because these could not be resolved spectroscopically. Table I lists the various spectroscopic branches of the $A \leftarrow X$ electronic transition that are available to collect the ion images. The symmetry index ϵ in Table I relates to the parity of a rotational state[37] as

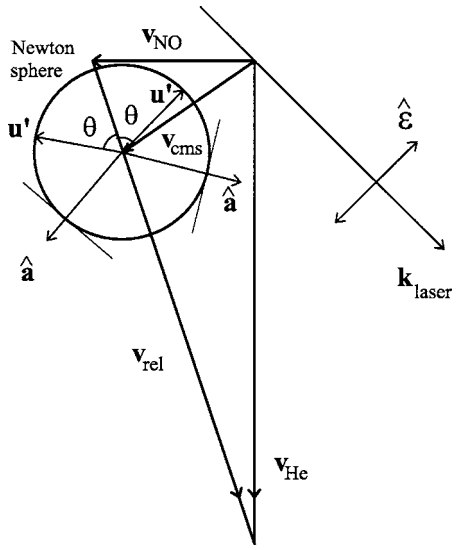

FIG. 8. Newton diagram for He–NO collisions to illustrate the effect of alignment on the detection probability. The vectors labelled with $\boldsymbol{u}'$ indicate scattering with a velocity in the center-of-mass frame under an angle θ. Remind that scattering is symmetric in respect to the relative velocity. The kinematic apse orientations corresponding to the drawn scattering vectors are indicated with $\hat{\boldsymbol{a}}$. A thin line is drawn perpendicular to $\hat{\boldsymbol{a}}$ in order to indicate the plane (perpendicular to the paper) in which the vector $\Delta \boldsymbol{j}$ is found. The propagation and polarization directions of the 226 nm laser are indicated in the figure with $\boldsymbol{k}_{laser}$ and $\hat{\boldsymbol{\epsilon}}$. The center-of-mass originis shifted downwards along v_{rel} (by 0.07 v_{rel}) of to enhance the readability of the figure. This leads to a Newton sphere that is too large.

$$p = (-1)^{j-\epsilon/2}. \tag{6}$$

The symmetry index ϵ is -1 for the upper component (f) of the Λ-doublet and 1 for the lower (e) component. Note that the parity of states within one branch alternates with $\Delta j = j' - j$. For example, final states with even Δj from the R_{21} branch have the same parity as those with odd Δj in the P_{11} (and vice versa).

Taking a first look at the experimental images one notices that there is little contamination of the images due to background signal. The He beam is switched from "on" to "off" after 100 laser shots. This procedure is repeated typically 20 times. The images with the He beam off are subtracted from those with the He beam on. The excimer/dye laser system and general valves run at 10 Hz, consequently collecting an image takes approximately 7 min. Some of the highest rotational states ($\Delta j > 10$), however, required twice the integration time.

The hexapole state selector eliminates all but one quantum state from the NO molecular beam. The product images show little contamination with scattering from other states or with direct detection of uncooled molecules present in the NO beam. These conditions lead to particularly crisp images. Only for scattering into the lower Λ-doublet component of the lowest rotational state ($j' = 1/2$, $\epsilon' = 1$) the ion image shows a strong distortion in the forward direction due to

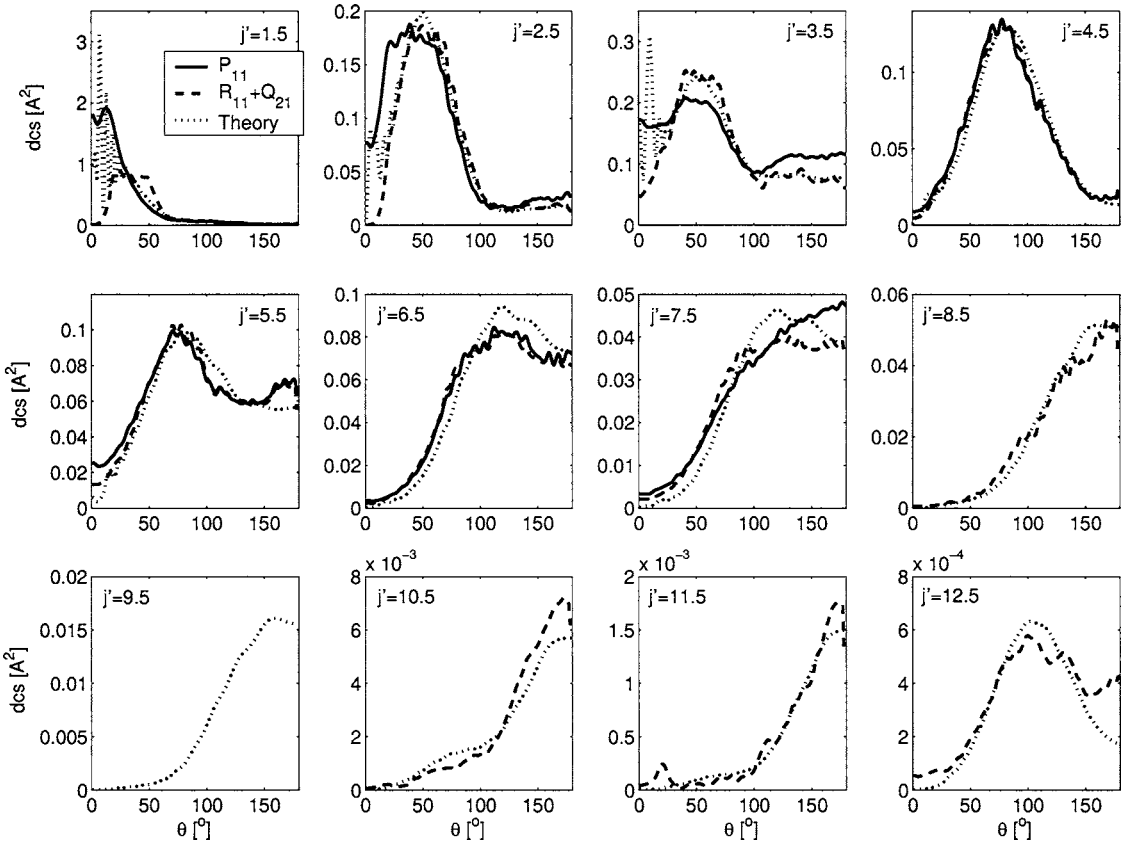

FIG. 9. Differential cross sections for spin-orbit conserving ($\bar{\Omega}' = 1/2$) transitions into the lower component of the Λ-doublet ($\epsilon' = 1$). Experimental results are given for different branches and compared to HIBRIDON calculations. The ion-images from which these differential cross sections are derived, are shown in Figs. 4 and 5. Note that both theory and experiment show sideways scattering for $j' = 12.5$ ($\bar{\Omega}' = 1/2$, $\epsilon' = 1$) while one would expect strong backward scattering for such a high rotational state. To transfer a substantial amount of translational energy into rotation, collisions with reversed momentum are usually preferred.

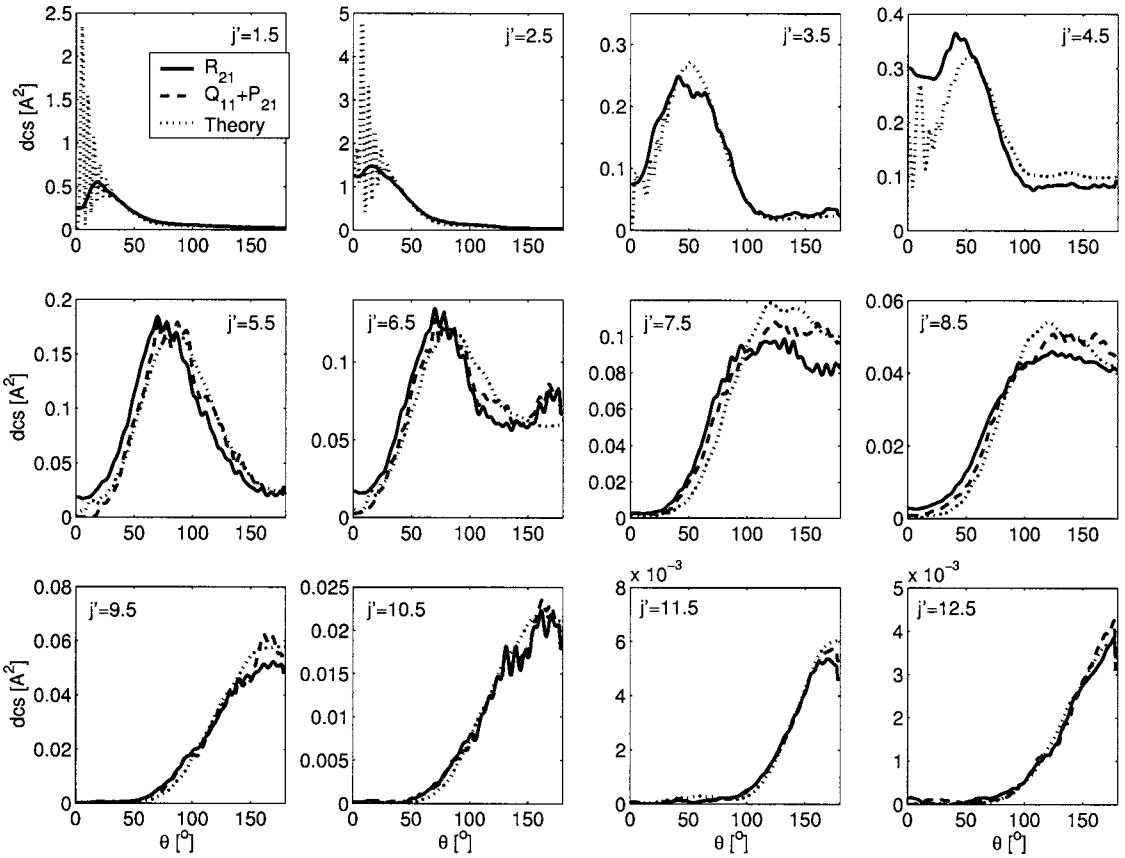

FIG. 10. Differential cross sections for $\bar{\Omega}'=1/2$, $\epsilon'=-1$. Experimental results are given for different branches and compared to HIBRIDON calculations. The ion-images from which these differential cross sections are derived, are shown in Figs. 4 and 5.

some residual NO in this state in the molecular beam (see Fig. 7). Because of this distortion it has not been used to extract a differential cross section and is not plotted in Fig. 5. For scattering into all higher rotational states this effect caused no problems.

The overall behavior of the images is as expected. For low rotational states, forward scattering dominates, while images for high rotational states show mostly backward scattering. In order to transfer more translational energy into rotation, collisions yielding a reversal of momentum are preferred. The only exception to this behavior is the $j'=12.5$ image in the $R_{11}+Q_{21}$ branch that shows sideways scattering, while the images for $j'=10.5$ and $j'=11.5$ only show backward scattering. The diameter of the projected scattering spheres decreases with j': The amount of translational energy after collision has to decrease if the amount of rotational energy increases. The radii of the projected spheres correspond well to this energy loss. This confirms the correctness of the velocity calibration. Images for scattering into $\bar{\Omega}'=3/2$ states (spin-orbit changing collisions) show more forward scattering than spin-orbit conserving collisions ($\bar{\Omega}'=1/2$). This might be explained assuming that spin-orbit changing collisions are particularly sensitive to the attractive part of the potential.

The uncorrected images from single P and R branches are reasonably symmetric in the relative velocity vector, while those for Q branches (combined with a P or R branch) show significant asymmetry. In each case, the left side of the ion images from Q branches shows less intensity than the right side (see Figs. 4–6). The images have been collected within a period of about three days, not in a particular order and the laser bandwidth is relatively large compared to the differences in NO center-of-mass velocities. This rules out Doppler effects as well as the spatial overlap of the lasers and the other beams as a possible reason for the asymmetry stated above. Collision-induced rotational alignment is the prime suspect for the effect. A qualitative classical explanation of this effect is described here.

In Fig. 8 the vectors labeled $\boldsymbol{u}'$ indicate scattering under an arbitrary angle θ. The corresponding kinematic apse $\hat{\boldsymbol{a}}$ is also drawn in the figure. The momentum component that is transformed into rotation ($\Delta\boldsymbol{p}=\boldsymbol{p}'-\boldsymbol{p}$) points along the kinematic apse $\hat{\boldsymbol{a}}$

$$\hat{\boldsymbol{a}} \equiv \frac{\boldsymbol{p}'-\boldsymbol{p}}{|\boldsymbol{p}'-\boldsymbol{p}|}, \tag{7}$$

where $\boldsymbol{p}$ and $\boldsymbol{p}'$ denote the linear momenta before and after collision, respectively. When the collision is impulsive and takes place very rapidly, there is essentially no change in the collision geometry during the time interval in which the intermolecular forces act. The internuclear distance $\boldsymbol{R}$ between the scattering partners remains unchanged during this interval. Conservation of total angular momentum yields a simple relation for the transferred amount of rotational angular momentum[25,38]

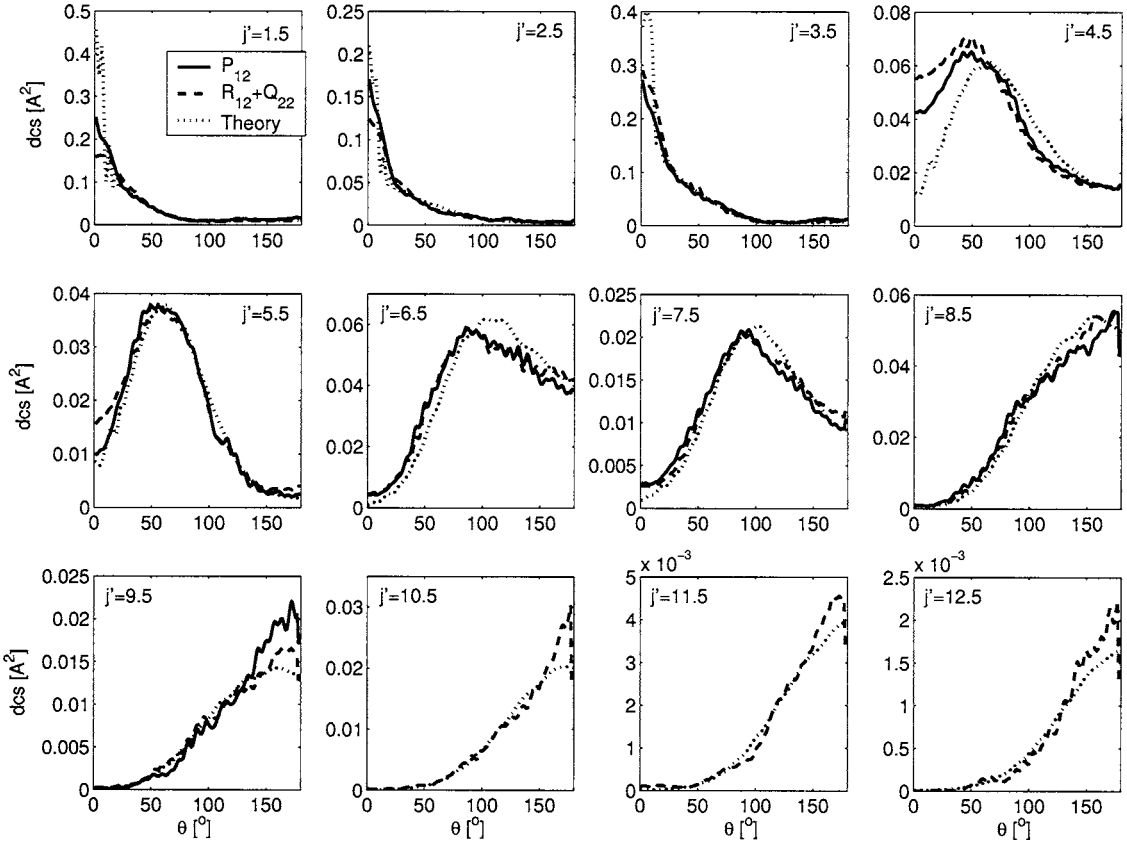

FIG. 11. Differential cross sections for spin-orbit changing ($\bar{\Omega}'=3/2$) transitions into the lower component of the Λ-doublet ($\epsilon'=1$). Experimental results are given for different both branches and compared to HIBRIDON calculations. The ion-images from which these differential cross sections are derived, are shown in Fig. 6.

$$\Delta \boldsymbol{j} = -\Delta(\boldsymbol{R}\times\boldsymbol{p}) = -(\boldsymbol{R}\times\Delta\boldsymbol{p}). \tag{8}$$

It follows directly that $\Delta\boldsymbol{j}\perp\Delta\boldsymbol{p}$. In quantum mechanical terms this means that $m_a=m_a'$. For the repulsive He–NO collision system this is expected to be an excellent approximation.

To reach qualitative understanding of the alignment effects in the ion-images, we assume for now that $\boldsymbol{j}'\approx\Delta\boldsymbol{j}$. This is only correct for $\Delta j\to\infty$. A quantitative treatment (at arbitrary j') as used to correct the ion-images is found in Appendix B. For Q branch transitions, the transition dipole moment $\boldsymbol{\mu}$ points parallel to the rotational angular momentum vector ($\boldsymbol{\mu}\|\boldsymbol{j}'$). The detection probability as a function of the angle between $\boldsymbol{j}'$ and the laser polarization $\hat{\boldsymbol{\epsilon}}$ for a Q branch transition is given by:[39]

$$|\hat{\boldsymbol{\mu}}\cdot\hat{\boldsymbol{\epsilon}}|^2 = |\hat{\boldsymbol{j}}'\cdot\hat{\boldsymbol{\epsilon}}|^2. \tag{9}$$

For a P or R branch transition $\boldsymbol{\mu}$ points perpendicularly to $\boldsymbol{j}'$, which leads to a reversed dependence of the detection probability upon the angle between $\boldsymbol{j}'$ and $\hat{\boldsymbol{\epsilon}}$[39]

$$|\hat{\boldsymbol{\mu}}\cdot\hat{\boldsymbol{\epsilon}}|^2 = \tfrac{1}{2}(1-|\hat{\boldsymbol{j}}'\cdot\hat{\boldsymbol{\epsilon}}|^2). \tag{10}$$

The laser light is polarized horizontally, bisecting the direction of the NO and He beams (see Fig. 8). In this figure, a thin line is drawn perpendicularly to $\hat{\boldsymbol{a}}$ in order to indicate the plane (perpendicular to the paper) in which $\boldsymbol{j}'$ is isotropically distributed. Note that since $\boldsymbol{j}'$ is isotropically distributed in that plane, $0\leqslant|\hat{\boldsymbol{j}}'\cdot\hat{\boldsymbol{\epsilon}}|^2\leqslant\frac{1}{2}$. It immediately follows that the alignment dependence for detection via a Q branch transition is stronger than in the case of a P or R branch transition. In the left-scattered case in Fig. 8, $\hat{\boldsymbol{\epsilon}}$ and $\boldsymbol{j}'$ are nearly perpendicular resulting in a low intensity for a Q branch transition and a high intensity for a P or a R branch transition. In the right side of the images, where $\hat{\boldsymbol{\epsilon}}$ and $\boldsymbol{j}'$ have larger parallel components, this effect is the other way around.

The raw experimental ion images for P and R branches are already near-symmetric in the relative velocity without correction (Figs. 4 and 6). This is because the detection probability due to the velocity of the molecules after collision and that due to alignment (Appendixes A and B) more-or-less cancel for detection via these branches. No saturation correction has to be applied for these branches to reproduce the experimental ion images with the simulated ones. The left side of the images corresponds to a larger laboratory velocity and thus to a lower detection probability than the right side. This is of course independent of the used spectroscopic branch. Roughly speaking, for P and R branch transitions the detection probability on the left side of the images is larger than on the right side, for Q branch transitions this effect is reversed. This makes ion images using a Q branch transitions for excitation strongly asymmetric as the detection probabilities due to alignment and due to the velocity of the molecules add, while when using P and R branch transitions they nearly cancel. The asymmetry is weakened because each absorption line in a Q branch coincides with one in a P or R branch, but the latter ones are generally weaker. In order to reproduce experimental ion-images obtained using the $P+Q$ and $R+Q$ branches, some saturation has been assumed. This is easily

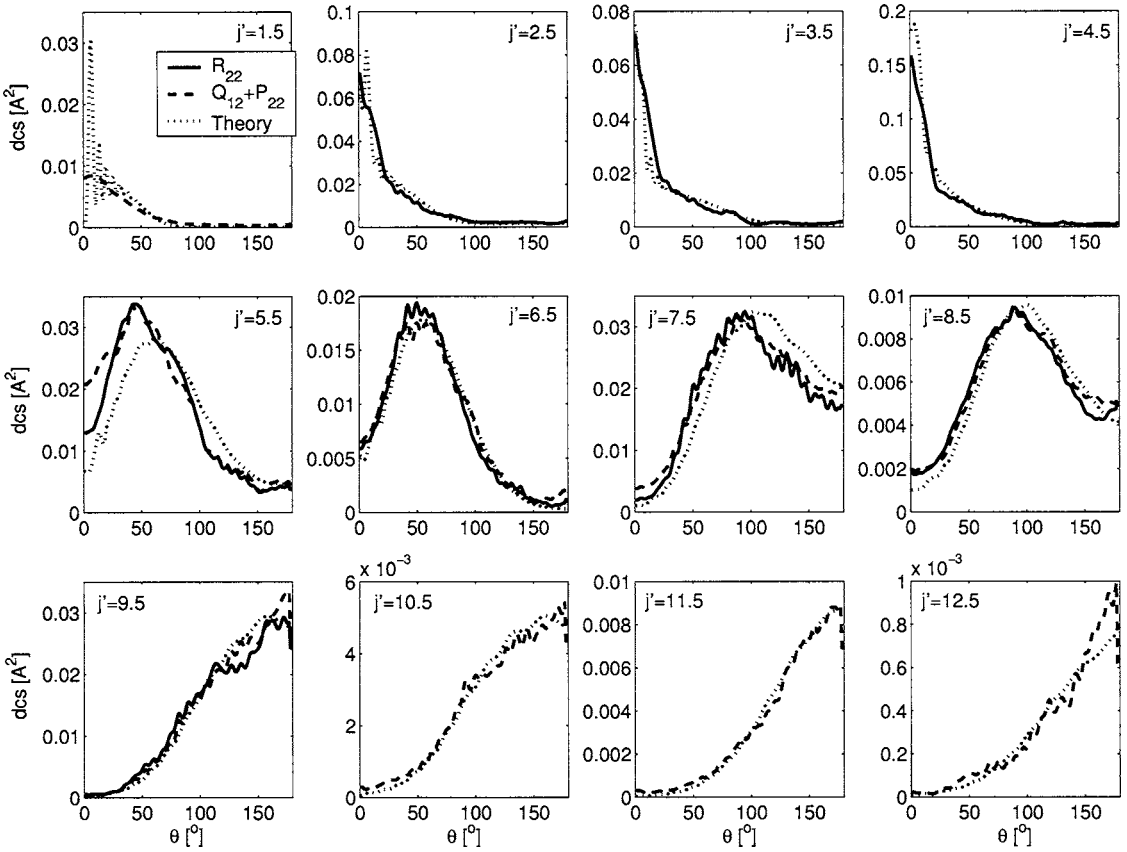

FIG. 12. Differential cross sections for $\bar{\Omega}'=3/2$, $\epsilon'=-1$. Experimental results are given for different branches and compared to HIBRIDON calculations. The ion-images from which these differential cross sections are derived, are shown in Fig. 6.

explained because these (combined) branches are stronger than single *P* and *R* branches. In Appendix B (Fig. 15) it was already shown that a *P* branch at low rotational states shows slightly more asymmetry than a *R* branch. This small effect is also seen in the experimental (and simulated) results in Fig. 4, which supports exploiting m_a conservation (along the apse) for collision-induced alignment correction.

The differential cross sections that have been obtained from all ion-images are plotted and compared to theory in Figs. 9–12. The theoretical results are from new close coupling HIBRIDON[31] calculations on restricted coupled-cluster single double triple [RCCSD(T)] potential energy surfaces.[30] Because the experiment does not provide total cross sections, experimental results have been normalized on the integral cross section obtained from the current HIBRIDON calculations

$$\sigma_{j,\bar{\Omega},\epsilon\rightarrow j',\bar{\Omega}',\epsilon'}=\int_0^{\pi}\mathrm{DCS}_{j,\bar{\Omega},\epsilon\rightarrow j',\bar{\Omega}',\epsilon'}\sin(\theta)d\theta. \qquad (11)$$

For the final states that have been studied using two different branches, both experimental differential cross sections are plotted as this gives information on the correctness of the extraction routine and the error in the measurements in general. Overall there is good agreement between theory and experiment and between the experimental results of different branches, indicating the high quality of the PESs and supporting the current extraction method including the apse based alignment correction (see Sec. III).

The substantial differences between theory and experiment as in Ref. 19 might be explained by a combination of theoretical and experimental factors. As discussed by De Lange *et al.*,[4] the anisotropy of the currently used RCCSD(T) potential energy surface is stronger than that of the CEPA surface used in Ref. 19. However, the observed discrepancies in Ref. 19 cannot be fully contributed to theory.[4] Excellent state selection and the correction for collision-induced alignment improves the reliability of the current experimental differential cross sections compared to those in Ref. 19. However, the current differential cross sections cannot directly be compared to the experimental results in Ref. 19 as the current results originate from the scattering out of the upper component of the Λ-doublet. In the experiment in Ref. 19, both components are equally present before collision.

Large differences are both observed and calculated between scattering into a $j',\epsilon'=-1$ and a $j',\epsilon'=1$ state for both spin-orbit changing and spin-orbit conserving collisions. Scattering into the $\epsilon'=1$ component of the Λ-doublet favors larger scattering angles than scattering into the $\epsilon'=-1$ component at the same j'. These differences have not been observed before and this is the first experiment that enables such a study. Scattering into the $\epsilon'=1$ state (lower component of the Λ-doublet) appears to yield the same ion-image (and a similar differential cross section) as scattering into the $\epsilon'=-1$ state (upper component of the Λ-doublet) with one less quantum of rotational angular momentum j'. The differential cross section for scattering into a $j'=n$, ϵ'

$=1$ is similar to that of a $j'=n+1$, $\epsilon'=-1$ final state. This effect cannot be explained by the small energy splitting between the two components of the Λ-doublet, for $\bar{\Omega}'=1/2$ ranging from ~ 0.01 cm^{-1} for low to 0.1 cm^{-1} for high rotational states in this study. For $\bar{\Omega}=3/2$ it ranges approximately from 4×10^{-5} cm^{-1} to 0.01 cm^{-1}. This leaves only a quantum mechanical effect to explain this observation, that will be addressed in Ref. 40.

Some differences between experiment and theory are seen for low rotational states. Theoretical differential cross sections show rapid oscillations in the forward direction (close to $\theta=0$) that are not seen in the experimental outcome. These oscillations are due to diffraction and the experimental resolution is too low to resolve these oscillations. Besides this, it is consistently found—independent of spin-orbit changing or conserving collisions—that the differential cross section for the first sideways scattered rotational state is predicted by theory to be less forward scattered than the experiment shows. These four differential cross sections are the only ones where a significant difference between experiment and theory exists. A slight underestimation of the attractive part of the PESs might cause this difference, but it cannot be fully excluded to be due to experimental artifacts. The forward direction is suspected to cause some problems during extraction of differential cross sections as the direction of the apse there is poorly defined. On the other hand, if the apse model fails, one also expects this to happen for the lowest rotational states, which is not the case. Except for these small differences, there is good agreement between theory and experiment.

VI. CONCLUDING REMARKS

For the first time, quantum-state-resolved differential cross sections arising from single parity states have been recorded. The differential cross sections are plotted in Figs. 9–12. A 2 meter long hexapole state selector was used to select the upper component of the Λ-doublet of the lowest rotational state ($j=1/2$, $\bar{\Omega}=1/2$, $\epsilon=-1$) from a molecular NO beam expansion. The fully state-selected beam was crossed with a helium beam and velocity-mapped ion-imaging was applied to record ion-images. The absence of molecules in other rotational states in the molecular beam due to hexapole focusing leads to particularly crisp images.

The present work provides the first experimental evidence for differences in the differential cross section between parity-breaking and parity-conserving transitions. We find that scattering into the $\epsilon'=1$ component of the Λ-doublet favors larger scattering angles than scattering into the $\epsilon'=-1$ component at the same j'. The differential cross sections for scattering into the lower component of the Λ-doublet $j=1/2$, $\epsilon=-1\rightarrow j'=n$, $\epsilon=1$ is very similar to that of scattering into the upper component $j=1/2$, $\epsilon=-1\rightarrow j'=n+1$, $\epsilon=-1$. These final states carry the same parity. The energy splitting between the two components of the Λ-doublet is too small to explain this observation.

We exploit m conservation along the kinematic apse during collision to correct for collision-induced alignment. A straightforward method to take this alignment into account is presented. The experimental results support this method. The distortion of the ion-images is well reproduced and differential cross sections for scattering into the same rotational state, extracted from different spectroscopic branches, correspond nearly perfectly to each other.

The experimental differential cross sections correspond well to those calculated in coupled channel (HIBRIDON) calculations based on RCCSD(T) potential energy surfaces (PESs).[41] Together with a previous experiment where steric asymmetries for collisions of He with (oriented) NO were measured,[4] this forms a thorough test for the ground electronic state PESs. The PESs are accurate in the energy range that is probed in these experiments ($E_{\mathrm{tr}}<510$ cm^{-1}). However, a slight underestimation of forward scattering for a few rotational states might be caused by underestimation of the attractive part of the PESs.

ACKNOWLEDGMENTS

The authors are very grateful to Professor Dr. A. W. Kleyn for his experimental support and to Rob Kortekaas for technical support. The Netherlands Organization for Scientific Research (NWO) is gratefully acknowledged for financial support through CW and FOM. D. W. Chandler and A. Gijsbertsen acknowledge NWO to enable this collaborative study by a visitor and a visiting grant, respectively. A. Gijsbertsen thanks M. S. Elioff, E. A. Wade, and M. P. J. van der Loo for helpful discussions.

APPENDIX A: VELOCITY CORRECTION

It is assumed that the NO detection probability ($T(x,y)$) due to the molecular residence time in the detection volume is inversely proportional to the absolute value of the velocity in the laboratory frame. The coordinates (x,y) indicate the position position on the detector in pixels and relate directly to the x and y components of the velocity in the center-of-mass (u'_x and u'_y) frame via the resolution G ($x=u'_x/G$ and $y=u'_y/G$)

$$T(x,y)\equiv\frac{1}{|\boldsymbol{v}'|}\Bigg/\left\langle\frac{1}{|\boldsymbol{v}'|}\right\rangle. \tag{A1}$$

Normalization is obtained by dividing with the average over all pixels ($\langle 1/|\boldsymbol{v}'|\rangle$).

The velocity in the laboratory frame can be approximated for each pixel in the ion-images, assuming an ideal velocity distribution in the beams. The velocity in the lab frame follows as:

$$\boldsymbol{v}'=\boldsymbol{v}_{\mathrm{cms}}+\boldsymbol{u}'. \tag{A2}$$

The absolute value of the velocity in the center-of-mass frame $|\boldsymbol{u}'|$ follows from energy conservation. It is dependent on the rotational state after collision j'. The components u'_x and u'_y in x and y direction (along the NO and He velocity vector, respectively) are defined by the position (x,y) on the detector and the resolution G. The component u'_z can now be specified as

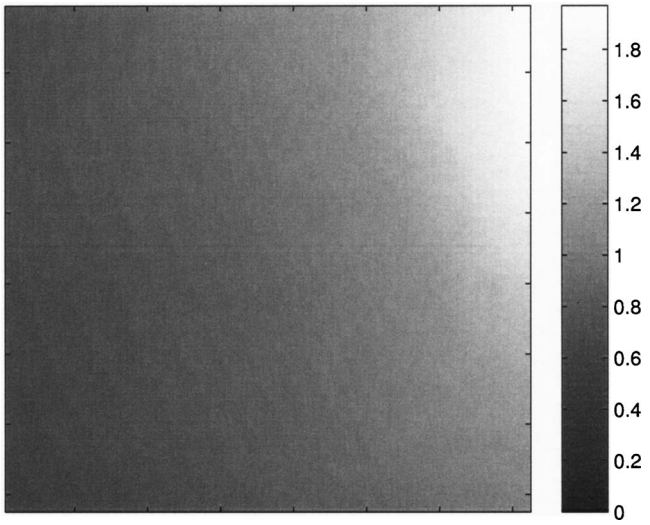

FIG. 13. The laboratory velocity detection probability $T(x,y)$, at each position on the image (here for $j'=4.5$) is given by the intensity. Molecules with low laboratory velocity remain in the detection volume for a longer time and are thus more likely to be detected than fast molecules. The frame of this figure corresponds to the dashed square in Fig. 3, which corresponds to the area of the ion-images in Figs. 4–6. Note that values of $T(x,y)<0.8$ do not occur within the frame.

$$u_z' = \sqrt{|\boldsymbol{u}'|^2 - u_x'^2 - u_y'^2}. \tag{A3}$$

For positions on the detector (x,y) where $|\boldsymbol{u}'|^2 - u_x'^2 - u_y'^2 < 0$, we will use $u_z'=0$. The center-of-mass velocity $\boldsymbol{v}_{\mathrm{cms}}$ is given by

$$\boldsymbol{v}_{\mathrm{cms}} = \boldsymbol{v}_{\mathrm{NO}} + \frac{m_{\mathrm{He}}}{m_{\mathrm{NO}}+m_{\mathrm{He}}}(\boldsymbol{v}_{\mathrm{He}} - \boldsymbol{v}_{\mathrm{NO}}). \tag{A4}$$

The laboratory velocity now follows as:

$$\boldsymbol{v}' = \begin{pmatrix} v_{\mathrm{NO}} \\ 0 \\ 0 \end{pmatrix} + \frac{m_{\mathrm{He}}}{m_{\mathrm{NO}}+m_{\mathrm{He}}} \begin{pmatrix} -v_{\mathrm{NO}} \\ v_{\mathrm{He}} \\ 0 \end{pmatrix} + \begin{pmatrix} u_x' \\ u_y' \\ \sqrt{|\boldsymbol{u}'|^2 - u_x'^2 - u_y'^2} \end{pmatrix}, \tag{A5}$$

with an absolute value of

$$|\boldsymbol{v}'| = \left[\left(v_{\mathrm{NO}} - \frac{m_{\mathrm{He}} v_{\mathrm{NO}}}{m_{\mathrm{NO}}+m_{\mathrm{He}}} + u_x' \right)^2 + \left(\frac{m_{\mathrm{He}} v_{\mathrm{NO}}}{m_{\mathrm{NO}}+m_{\mathrm{He}}} + u_y' \right)^2 + |\boldsymbol{u}'|^2 - u_x'^2 - u_y'^2 \right]^{1/2}. \tag{A6}$$

Equation (A5) can be extended to correct for the Doppler shift, but because of the small center-of-mass velocity differences of the scattered molecules this is not done here. As an example, the detection probability factor for $j'=4.5$ as derived from Eq. (A1) is plotted in Fig. 13. From this figure it can be seen that for the current images, $T(x,y)$ turns out to be a factor of 2 larger in the top-right angle than in the bottom-left angle of the images. This is a substantial effect that cannot be neglected in extracting differential cross sections from ion-images.

APPENDIX B: COLLISION-INDUCED ALIGNMENT

A simple but widely applicable correction treatment based on the m conservation along the kinematic apse is derived here. The alignment dependent detection probability is proportional to

$$S_a(j' \rightarrow j^*) \equiv \sum_{m^*} |\langle \Psi^*(j^*,m^*)|\hat{\boldsymbol{\mu}}\cdot\hat{\boldsymbol{\varepsilon}}|\boldsymbol{R}(\beta_p)\Psi_a'(j',m_a')\rangle|^2. \tag{B1}$$

The wave functions will be referred to as $\Psi_a(j=1/2, m_a = \pm 1/2)$, $\Psi_a'(j',m_a')$ and $\Psi^*(j^*,m^*)$, denoting, respectively, the rotational states before collision, after collision (in the apse frame) and after laser excitation to the $^2\Sigma$ state. Note that m^* is defined along the electric field of the linearly polarized laser (laser frame). The wave function in the apse system $\Psi_a'(j',m_a')$ is transformed into the laser frame, the angle between the laser polarization and the kinematic apse is described as β_p. During excitation to the $^2\Sigma$ state the projection of the rotational angular momentum in the laser frame remains conserved. The wave function after a collision will be aligned due to the collision. If one assumes that the projection m_a of the total angular momentum $\boldsymbol{j}$ on the kinematic apse is conserved during collision, it is relatively easy to take this effect into account. The kinematic apse direction is given by

$$\hat{\boldsymbol{a}} = \frac{\boldsymbol{k}'-\boldsymbol{k}}{|\boldsymbol{k}'-\boldsymbol{k}|}, \tag{B2}$$

where $\boldsymbol{k}$ and $\boldsymbol{k}'$ denote the momentum vectors before and after collision, respectively. Khare[25] and Meyer[26] showed that m_a conservation along the kinematic apse is a reasonable approximation. Rotation of the wave function $\Psi_a'(j',m_a')$ over the angle between the apse and the laser polarization β_p provides the aligned wave function in the laser frame

$$\boldsymbol{R}(\beta_p)\Psi_a'(j',m_a) = \sum_{m'} d^j_{m',m_a}(\beta_p)\Psi'(j',m'). \tag{B3}$$

Note that $0 \leqslant \beta_p \leqslant 90°$. Substitution of Eq. (B3) into Eq. (B1) gives

$$S_a(j' \rightarrow j^*) = \sum_{m'} |d^j_{m',m_a}(\beta_p)\langle \Psi^*(j^*,m^*)|\hat{\boldsymbol{\mu}}\cdot\hat{\boldsymbol{\varepsilon}}|\Psi'(j',m')\rangle|^2. \tag{B4}$$

In order to distinguish between the apse alignment dependent detection probability and the ordinary Hönl-London factors, these are, respectively, written as $S_a(j' \rightarrow j^*)$ and $S(j' \rightarrow j^*)$. Jacobs and Zare[42] show that the (m-dependent) detection probability or rate constant for linearly polarized light is proportional to the well-known Hönl-London factors multiplied with a 3-j symbol:

$$|\langle \Psi^*(j^*,m^*)|\hat{\boldsymbol{\mu}}\cdot\hat{\boldsymbol{\varepsilon}}|\Psi'(j',m')\rangle|^2 = S(j' \rightarrow j^*) \begin{pmatrix} j^* & 1 & j' \\ m' & 0 & -m' \end{pmatrix}^2 \delta_{m^*,m'}. \tag{B5}$$

The Hönl-London factors $S(j' \rightarrow j^*)$ for a $^2\Sigma \leftarrow {}^2\Pi$ transition

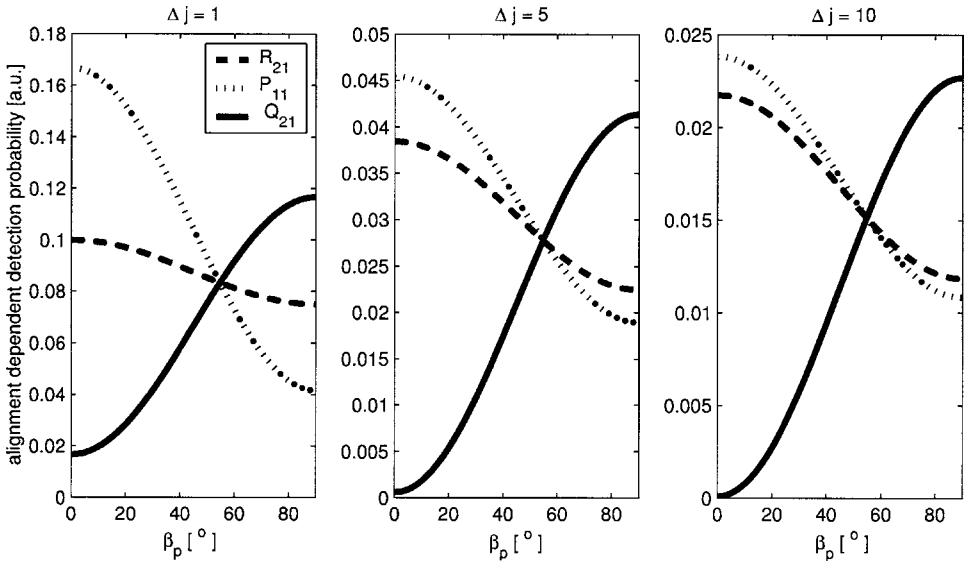

FIG. 14. The alignment dependent detection probability $(S_a(j' \to j^*)/S(j' \to j^*))$ is plotted against the angle β_p between the apse and the laser polarization for three different values of Δj and for three different branches.

where first derived by Earls[43] and are also available from Ref. 44. Together this gives:

$$S_a(j' \to j^*) = S(j' \to j^*) \sum_{m'} \left| d^j_{m',m_a}(\beta_p) \begin{pmatrix} j^* & 1 & j' \\ m' & 0 & -m' \end{pmatrix} \right|^2 . \tag{B6}$$

Note that the detection probability is independent of the sign of m_a. Equation (B6) provides a novel and simple method to correct ion-images for collision-induced alignment. Every pixel on an image corresponds to a certain final momentum (velocity). With the final rotational state defined and therefore the final velocity of the NO molecules defined, each position on the detector can be associated with a particular kinematic apse via Eq. (B2). Figure 14 shows the dependence of the detection probability (divided by the Hönl-London factor) $S_a(j' \to j^*)/S(j' \to j^*)$ on the angle β_p between the apse and the electric field of the laser. This is plotted for three different Δj, for a Q, an R and a P branch transition. Already at $\Delta j = 10$, the expected limiting behavior for $j' \to \infty$ emerges, as argued in Sec. V below Eqs. (9) and (10). In Fig. 15 the detection probability $S_a(j' \to j^*)$ is given for four branches and one rotational state. The size of the images in Fig. 15 corresponds to the size required to record an entire ion-image of the scattered NO product. Note that the Q_{11} strongly dominates over the P_{21} because its Hönl-London factor for the Q_{11} transition is about a factor of three larger than that for the P_{21} transition. The R_{11} and Q_{21} branches carry a similar value of the Hönl-London factor, but as expected the Q branch character dominates the alignment dependent detection probability. The alignment dependence of the detection probability for a Q branch transition is about a factor of two stronger than and opposite to that of a P or R branch transition. This is clearly demonstrated in Eqs. (9) and (10) and Fig. 14.

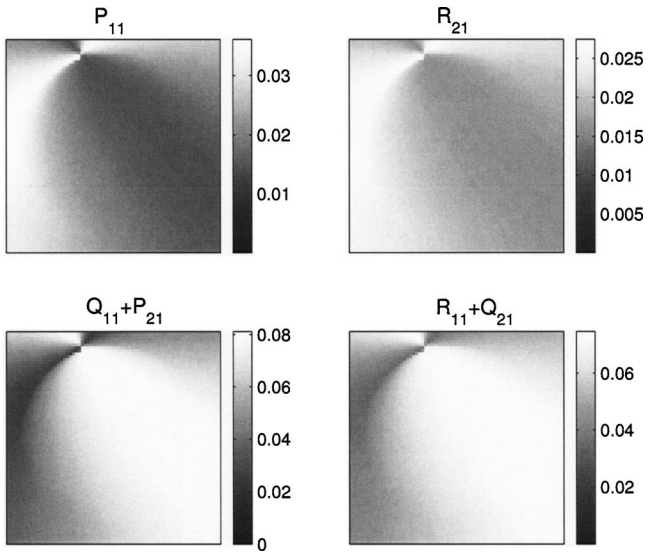

FIG. 15. The alignment dependent detection probability $S_a(j' \to j^*)$ at each position on the image (here for $j' = 4.5$) is given by the intensity for several branches. The angle between the apse and the laser polarization defines the detection probability via Eq. (B6). The size of each of the frames in this figure corresponds to the dashed square in Fig. 3, which corresponds to the frames of the ion-images in Figs. 4–6. Note that the apse is undefined when $\boldsymbol{k}' = \boldsymbol{k}$ [see Eq. (B2)]. The dynamic range of each of the images is taken from 0 to its maximum value.

In the event of full saturation of the $A \leftarrow X$ transition, the detection probability no longer depends on the scattering angle. In that case, correction of the ion-images with only the velocity correction should yield undistorted ion-images. If partial saturation occurs, the dependence of the detection probability on β_p becomes less.

$$S_{\text{sat}}(j' \to j^*) = S_0 + S_a(j' \to j^*). \tag{B7}$$

The parameter S_0 indicates the saturation: if $S_0 \ll S_a(j' \to j^*)$, there is no saturation, if $S_0 \gg S_a(j' \to j^*)$ there is full saturation and the detection probability no longer depends on the scattering angle. To get an idea of the effect of the saturation correction, S_0 can be expressed in terms of the value of $S_a(j' \to j^*)$ averaged over all pixels $\langle S_a(j' \to j^*) \rangle$.

[1] H. Joswig, P. Andresen, and R. Schinke, J. Chem. Phys. **85**, 1904 (1986).
[2] M. J. L. de Lange, M. Drabbels, P. T. Griffiths, J. Bulthuis, and J. G. Snijders, Chem. Phys. Lett. **313**, 491 (1999).
[3] M. J. L. de Lange, Ph.D. thesis, Vrije Universiteit Amsterdam (2003).
[4] M. J. L. de Lange, S. Stolte, C. A. Taatjes, J. Kłos, G. C. Groenenboom, and A. v.d. Avoird, J. Chem. Phys. **121**, 11691 (2004).
[5] A. G. Suits, L. S. Bontuyan, P. L. Houston, and B. J. Whitaker, J. Chem. Phys. **96**, 8618 (1992).
[6] A. T. J. B. Eppink and D. H. Parker, Rev. Sci. Instrum. **68**, 3477 (1997).
[7] K. T. Lorenz, M. S. Westley, and D. W. Chandler, Phys. Chem. Chem. Phys. **2**, 481 (2000).
[8] N. Yonekura, C. Gebauer, H. Kohguchi, and T. Suzuki, Rev. Sci. Instrum. **70**, 2365 (1999).
[9] A. A. Dixit, P. J. Pisano, and P. L. Houston, J. Phys. Chem. A **105**, 11165 (2001).
[10] K. T. Lorenz, D. W. Chandler, J. W. Barr, W. Chen, G. L. Barnes, and J. I. Cline, Science **293**, 2063 (2001).
[11] M. S. Elioff and D. W. Chandler, J. Chem. Phys. **117**, 6455 (2002).
[12] M. S. Elioff, J. J. Valentini, and D. W. Chandler, Science **302**, 1940 (2003).
[13] E. A. Wade, K. T. Lorenz, D. W. Chandler, J. W. Barr, G. L. Barnes, and J. I. Cline, Chem. Phys. **301**, 1 (2004).
[14] T. P. Rakitzis, A. J. van den Brom, and M. H. M. Janssen, Science **303**, 1852 (2004).
[15] *Imaging in Molecular Dynamics*, edited by B. Whitaker (Cambridge University Press, Cambridge, 2003).
[16] S. D. Jons, J. E. Shirley, M. T. Vonk, C. F. Giese, and W. R. Gentry, J. Chem. Phys. **105**, 5397 (1996).
[17] R. B. Gerber, V. Buch, U. Buck, G. Maneke, and J. Schleusener, Phys. Rev. Lett. **44**, 1397 (1980).
[18] R. Schinke, J. Chem. Phys. **73**, 12 (1980).
[19] M. S. Westley, K. T. Lorenz, D. W. Chandler, and P. L. Houston, J. Chem. Phys. **2**, 473 (2001).
[20] M. Yang and M. H. Alexander, J. Chem. Phys. **103**, 6973 (1995).
[21] H. Kohguchi, T. Suzuki, and M. H. Alexander, Science **294**, 832 (2001).
[22] F. Harren, D. H. Parker, and S. Stolte, Comments At. Mol. Phys. **26**, 109 (1991).
[23] J. L. van Leuken, J. Bulthuis, S. Stolte, and J. G. Snijders, Chem. Phys. Lett. **260**, 595 (1996).
[24] J. I. Cline, K. T. Lorenz, E. A. Wade, J. W. Barr, and D. W. Chandler, J. Chem. Phys. **115**, 6277 (2001).
[25] V. Khare, D. J. Kouri, and D. K. Hoffmann, J. Chem. Phys. **74**, 2275 (1981).
[26] H. Meyer, J. Chem. Phys. **102**, 3151 (1995).
[27] Y. Kim, H. Meyer, and M. H. Alexander, J. Chem. Phys. **121**, 1139 (2004).
[28] M. J. L. de Lange, J. J. van Leuken, M. Drabbels, J. Bulthuis, J. G. Snijders, and S. Stolte, Chem. Phys. Lett. **294**, 332 (1998).
[29] A. E. Wiskerke, C. A. Taatjes, A. W. Kleyn, R. J. W. E. Lahaye, S. Stolte, D. K. Bronnikov, and B. E. Hayden, Faraday Discuss. **96**, 297 (1993).
[30] J. Kłos, G. Chalasinski, M. T. Berry, R. A. Kendall, R. Burcl, M. Szczesniak, and S. M. Cybulski, J. Chem. Phys. **112**, 4952 (2000).
[31] HIBRIDON is a package of programs for the time independent quantum treatment of inelastic collisions written by M. H. Alexander, D. E. Manolopoulos, H. J. Werner, and B. Follmeg, with contributions by P. F. Vohralik, D. Lemoine, G. Corey *et al.* More information and a copy of the code can be obtained from http://www.chem.umd.edu/physical/alexander/hibridon/.
[32] M. H. Alexander, J. Chem. Phys. **76**, 5974 (1982).
[33] M. H. Alexander, Chem. Phys. **92**, 337 (1985).
[34] G. C. Corey and M. H. Alexander, J. Chem. Phys. **85**, 5652 (1986).
[35] M. H. Alexander, J. Chem. Phys. **111**, 7426 (1999).
[36] A. Gijsbertsen, M. J. L. de Lange, A. E. Wiskerke, H. Linnartz, M. Drabbels, J. Kłos, and S. Stolte, Chem. Phys. **301**, 293 (2004).
[37] J. M. Brown, J. T. Hougen, K. P. Huber *et al.*, J. Mol. Spectrosc. **55**, 500 (1975).
[38] D. J. Kouri and D. K. Hoffman, Theor. Chem. Acc. **103**, 281 (2000).
[39] D. A. Case, D. G. M. McClelland, and D. R. Herschbach, Mol. Phys. **35**, 54 (1978).
[40] A. Gijsbertsen, H. V. Linnartz, C. A. Taatjes, and S. Stolte (in preparation).
[41] J. Kłos, G. Chalasinski, M. T. Berry, R. Bukowski, and S. M. Cybulski, J. Chem. Phys. **112**, 2195 (2000).
[42] D. C. Jacobs and R. N. Zare, J. Chem. Phys. **65**, 5457 (1986).
[43] L. T. Earls, Phys. Rev. **48**, 423 (1935).
[44] R. N. Zare, *Angular Momentum: Understanding Spatial Aspects in Chemistry and Physics* (Wiley, New York, 1988).